ELM and inter-ELM heat and particle flux to a secondary divertor in the DIII-D tokamak

To cite this article before publication: Renato Perillo *et al* 2021 *Nucl. Fusion* in press https://doi.org/10.1088/1741-4326/ac0f38

ELM and inter-ELM heat and particle flux to a secondary divertor in the DIII-D tokamak

R. Perillo[1], J.A. Boedo[1], C.J. Lasnier[2], D. L. Rudakov[1], T. Osborne[3], J. Watkins[4] and the DIII-D team.

[1] University of California, San Diego, 95000 Gillman Drive, La Jolla, CA 92130, USA
[2] Lawrence Livermore National Laboratory, Livermore, CA 94551, USA
[3] General Atomics, P.O. Box 85608, San Diego, CA 92186-5608, USA
[4] Sandia National Laboratories, Albuquerque, NM 87185, USA

Abstract

DIII-D ELMing discharges with a secondary X-point (XPT) inside the vessel were used to evaluate the power distribution between the primary and secondary divertors. The magnetic balance, defined by the distance between the primary and secondary separatrices at the outer midplane (dRsep), was varied from -5 mm (lower-single-null, LSN) to +16 mm (upper-single-null, USN).
We find that the secondary divertor receives up to 1/3 of the total heat flux (primary + secondary divertors), and it is dominated by the ELM-driven flux. Both the radially-integrated and the peak heat flux to the secondary divertor decay below ~50% of the maximum as dRsep is varied from -5 to +6mm, but the integrated heat flux decay flattens out and it would take dRsep above ~25mm to reduce the ELM heat flux to the secondary divertor below 10% of the one deposited to a well-defined SN.
Both the secondary inner and outer strike points receive heat flux during ELMs. The peak heat flux is comparable in both strike points for dRsep < 10mm, but the inner strike point receives less than 15% of the total flux. This is experimental evidence that the secondary inner divertor region receives significant ELM flux which should be taken into account for the design of future generation tokamaks.

1. Introduction

Edge-localized-modes (ELMs) are plasma instabilities[1] characteristic of high-energy confinement (H-mode) discharges[2] causing periodic loss of particles and energy from the confined plasma[3] into the scrape-off-layer (SOL) towards the plasma-facing-components (PFC)[4][5]. ELMs, which are a response from the plasma to the pedestal pressure build-up, remove plasma and impurities from the core, providing density pump out and preventing ash accumulation that would lead to reduced performance (see ref [6] and references therein) but they increase significantly the heat and particle load to the PFC.
To avoid critical heat flux (CFH) events, the peak power flux density for long-term quasi-stationary operation of the ITER[7] Tungsten (W) divertor PFC should not exceed ~20 MW/m^2[8]. The onset of bulk W surface melting occurs approximately at 28 MW/m^2[9] and exceeding such limit would lead to material degradation via formation of leading edges by redistributed melt, recrystallization and bubble formation[10]. Regarding transient events (such as ELMs), the critical W divertor melting threshold, expressed by

the 'heat flux factor'[11] and calculated as $F_{HF} = q_{\perp}\Delta t_{trans}^{-1/2}$ where $q_{\perp}$ is the perpendicular energy density to the target and Δt_{trans} the duration of the transient, is 50 $MJm^{-2}s^{-1/2}$[12].

Potential solutions and mitigation strategies to the quasi-stationary and transient power exhaust problem are currently being studied and include: 1) small ELM regimes (type II, III, V)[13], 2) ELM suppression by RMP coils[14] and 3) divertor configurations that increase the plasma-wetted area at the targets region i.e. snowflake[15][16], super-X divertor[17][18] and double null (DN) configurations[19].

ITER is designed to operate in lower single null (LSN) but with a secondary X-point (XPT) inside (or in close vicinity to) the vessel[20]. Since the presence of the null is expected to result in some heat flux to the upper section of the vessel, the wall has to be engineered to accept such power load. Measurements of ELM and inter-ELMs heat fluxes to the secondary XPT of today's tokamaks are essential to provide design guidance, given the uncertainties in the "Heat and Nuclear Load Specifications" (HNLS) extrapolations for ITER[21]. Moreover, next generation spherical tokamaks[22] are designed to operate in quasi-DN configuration. Therefore, there is a need to quantify the heat load that a secondary divertor receives during and in-between type-I ELMs.

Experiments evaluating divertor power sharing for different magnetic balances have been carried out at EAST tokamak, showing the effect of ∇B direction on active and secondary divertor asymmetry[23]. Heat flux footprint widths of type-III ELMs have been investigated[24], providing scaling laws of those scenarios for EAST. The influence of magnetic flux balance on divertor power sharing for ELMs-free discharges has been studied in Alcator C-MOD[25], while in MAST[26] the up-down heat flux asymmetry has been evaluated for one H-mode DN configuration. Measurements of the perpendicular heat flux decay length in the SOL during H-mode for both LSN and USN have been carried out at ASDEX-Upgrade[27], as well as power load deposition for USN and DN equilibria[28]. Research on advanced plasma scenarios at ASDEX-Upgrade and JET[29][30][31] showed the achievement of 'small' type II ELMs for discharges at high density, high triangularity and operating in DN. At DIII-D[32][33][34], peak heat flux in both active and secondary divertors have been measured for different magnetic balances (LSN to USN) together with their effect on discharge performance and SOL plasma characteristics.
However, most of the work reported above was carried out in L-mode, ELM-free regimes or without spatially and time-resolved divertor ELM heat flux footprints. The scope of this paper can then be summarized as follows:

(1) Evaluate heat and particle fluxes to the primary and secondary divertor in DIII-D during type-I ELMs and inter-ELMs.
(2) Quantify the power distribution between primary and secondary inner (ISP) and outer (OSP) strike points.
(3) Examine how variations of dRsep affect the above.

This work provides experimental results that can be of interest for the modeling community in order to extract predictions for future generation tokamaks[35].

2. Methods and experimental set up

The discharge evolution is shown in *figure 1*, where the time window used in this work is highlighted in yellow. Line averaged density is ~$6x10^{13}$ cm^{-3} (*Fig. 1a*), maximum stored energy W_{tot} is ~ 1 MJ (*Fig. 1b*), total plasma power P_{tot} is ~3.5 MW (*Fig. 1c*) and dRsep varies from -5 to ~+18 mm from shot to shot, as seen in *Fig. 1d*. D-α emissions measured at the lower outer divertor are shown in *Fig. 1e*. All discharges examined in this work are in attached conditions, with Greenwald fraction n/n_{GW}~0.5. Plasma current Ip is 1.2 MA and reversed (counter clock-wise when seen from above) Bt = 1.8T, with ∇B ion drift pointing to the upper divertor. ELM frequency for these shots is between 30-50 Hz and remains constant.

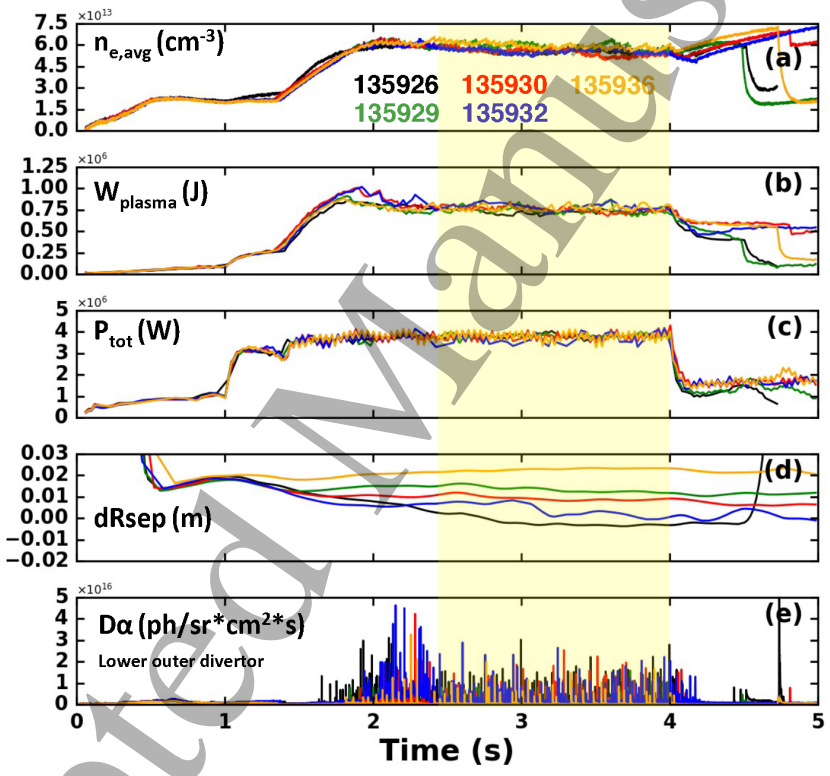

Figure 1 Discharge evolution of the shots studied in this work. (a) averaged electron density (b) total input power (c) stored plasma energy (d) dRsep (smoothed), up-down magnetic balance (e) D-alpha signal measured at the lower outer divertor. The area highlighted in yellow indicates the time window selected.

DRsep was varied while maintaining other parameters constant, as seen in *Fig 1*. In DIII-D, dRsep >2cm corresponds to an upper-single-null (USN), while dRsep <-2cm indicates a lower-single-null (LSN) and dRsep=0 corresponds to a double-null (DN). In this work, we adopt discharges with different degrees of magnetic balance in *quasi* DN configurations, with dRsep ranging from -5mm to +16mm. For clarity, discharges with dRsep<0 will be referred to as LSN, and when dRsep>0 as USN[33]. Although a LSN with dRsep=-5mm is not a 'well defined' LSN, and therefore some flux is channeled to the opposite divertor, we can estimate those losses by evaluating the heat flux to the secondary divertor for symmetric USN discharges. Two configurations with dRsep = -5

and +7 mm are shown in *Fig. 2a* and *2b* (the EFIT code[36] was used to reconstruct the equilibria). The dRsep values differ slightly between ELM and inter-ELM cases (see next section) due to the impossibility of maintaining a perfectly constant up-down magnetic balance throughout the whole shot. However, such variations are taken into account in the calculations.

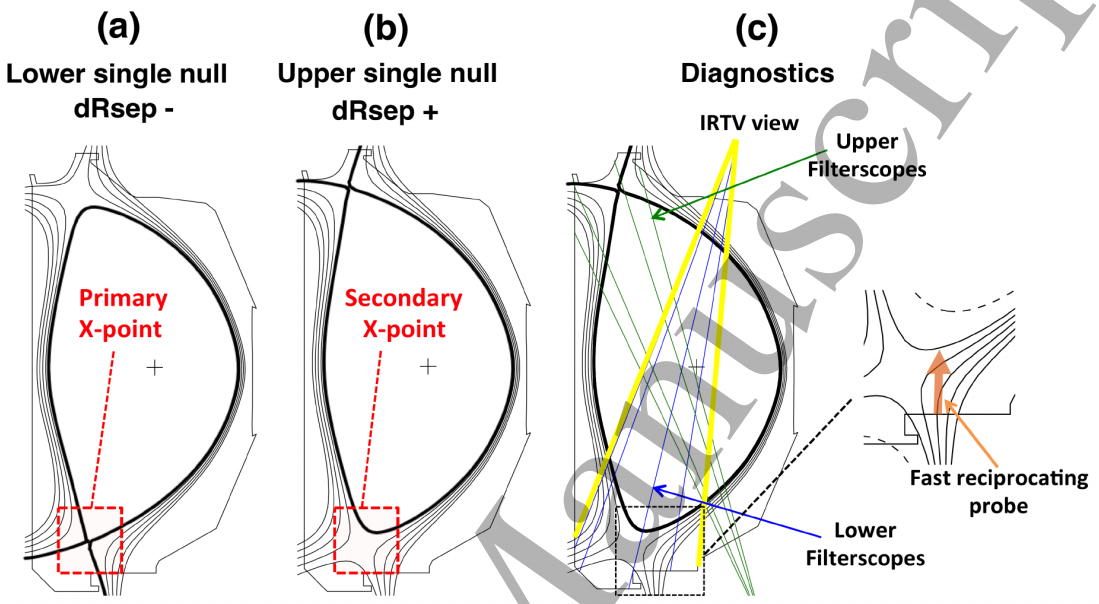

Figure 2 (a) Lower-single-null (LSN) configuration, with the secondary XPT at the upper divertor (b) Upper-single-null configuration, with the secondary XPT at the lower divertor (c) Diagnostics used in this work: IRTV view is indicated in yellow, upper divertor FS in green, lower divertor FS in blue and fast reciprocating probe in orange. The radial spacing between poloidal magnetic flux lines is 1 cm.

We have performed all the IRTV[37] measurements at the lower divertor (*Fig. 2c*, indicated in yellow) and the view of the camera, with a spatial resolution of 0.19 cm/pixel and time resolution of 4.83 kHz, covers both the inner and outer divertors. The surface temperature is collected applying an absolute calibration to the raw data during the baking of DIII-D at 350°C; camera data are then compared to the temperature of embedded thermocouples. Surface temperatures are converted to heat flux by using the code THEODORE[38], a 2D inverse heat transfer code.

A fast reciprocating probe (FRP)[39][40] located at the divertor floor and which extends up to ~20 cm vertically inside the vessel (*Fig. 2c*, orange) is used to measure profiles[41] of ion saturation current (I^+), T_e and n_e[42]. Probe signals are digitized at 2MHz.

Filterscopes (FS) have been used to measure D-alpha in the lower (*Fig. 2(c),* blue) and upper (*Fig. 2c,* green) divertors. The chords are absolutely calibrated and include the geometry[43].

3. Experimental results

3.1 Heat flux footprints

We first proceed to evaluate the relative contribution of the ELM and inter-ELM heat flux to the primary and secondary divertors, in particular the inner and outer divertor legs.

To separate the ELM from the inter-ELM heat flux, we use conditional averaging of the IRTV signal versus time over windows of typically ~ 1-2 ms, which correspond to the time range where the heat flux profile returns to pre-ELM levels, and we evaluate the ELM energy loss (ΔW_{ELM}) for each magnetic configuration using conditional averaging of the diamagnetic loop signal. Two representative cases, LSN and USN, are reported in *Fig. 3* together with D-α signal measured at the outer midplane for reference. To take into account the slightly different ELM sizes, shown in *Table 1*, we multiply each ELM heat flux by a correction coefficient (c in *Table 1*), calculated as $c_i = \frac{\Delta W_{ELM\ (AVG)}}{\Delta W_{ELM\ (i)}}$ where $\Delta W_{ELM\ (i)} = \frac{\sum_{ELM=1}^{n} \Delta W_{ELM}}{n}$ with n being the number of ELMs per each dRsep case i and $\Delta W_{ELM\ (AVG)}$ the averaged ELM energy loss for all the discharges adopted in this work i.e. 58.16 kJ, and we find the correction coefficients to be comparable within ~15%.

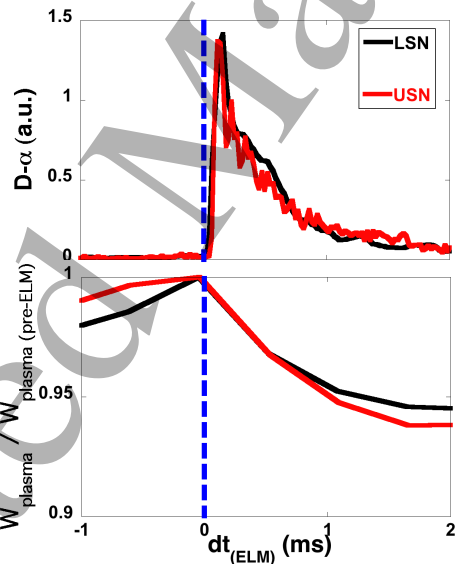

Figure 3 ELM D-α signal at the outer midplane (up) and ΔW_{plasma} normalized over the pre-ELM level (down) VS ELM time for two representative dRsep cases.

Table 1 ELM energy loss per each dRsep case (ΔW_{ELM}) and the respective correction factor (c).

dRsep (mm)	ΔW_{ELM} (kJ)	c
-5	59	0.986
-2.5	52	1.118
+4.5	61	0.953
+6	59	0.986
+9	60	0.969
+13	58	1.002
+16	58	1.002

The time evolution of the local heat flux at the secondary divertor strike points (OSP in red and ISP in blue) for a typical ELM pulse is presented in *Fig. 4* and it shows that the secondary ISP features ~65% of the heat flux at the OSP. 3D plots of the heat flux spatial profiles vs time at both inner and outer divertor are shown as insets. During the ELM, spatio-temporal structures (previously reported in the primary divertor[25][44][45]) develop at the secondary outer region (*Fig. 4*, upper-right inset) which extend outwards into the SOL and vanish as the ELM heat flux evolves and becomes localized solely at the strike point. The heat flux profile at the inner divertor (*Fig. 4*, bottom-right inset, where the SOL is on the left side of the peak and the PFR on the right) however, is well defined and no structures are present.

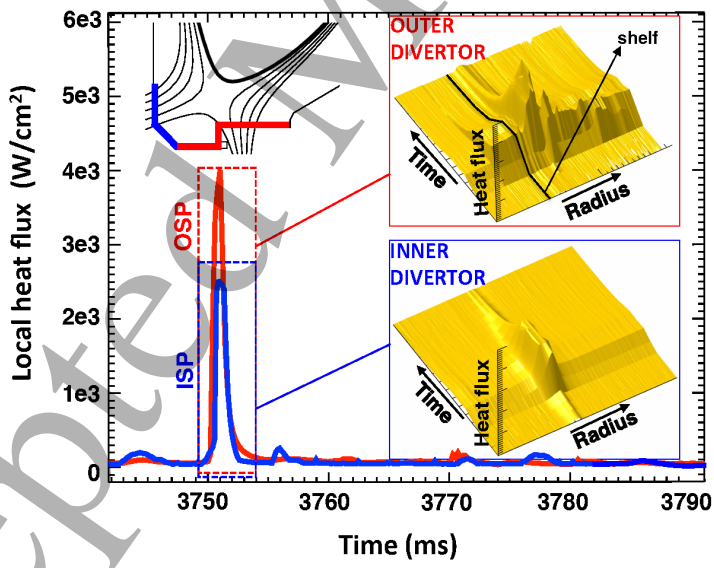

Figure 4 Local peak heat flux to secondary OSP (red) and ISP (blue) during an ELM. The upper-left inset shows the locations of the measurements in outer and inner divertor, and the up-right and bottom-right insets show a 3D representation of the heat flux profile evolution on those regions. Note that structures occur outward the outer strike point, while they are absent near the ISP.

The conditionally-averaged ELM heat flux radial profiles obtained by averaging over 5 ELMs and mapped at the outer midplane for comparison, are shown in *Fig. 5*. The OSP at the floor is near the edge of a step or "shelf" (see *Figs. 2* and *4* top left inset in red) that appears in the profiles as a small peak and a flat line and we do not include that

transitional data in any of our calculations or integrals. The heat flux is not zero far away from the strike points because there is always heating by radiation from the bulk plasma and in the case of the LSN, local radiation.

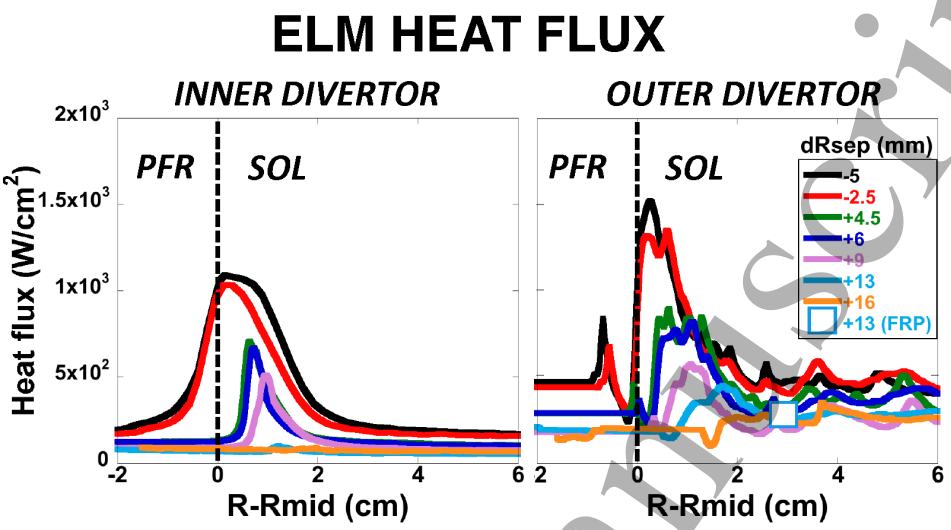

Figure 5 Lower divertor conditionally-averaged ELM heat flux at inner (left) and outer (right) divertor targets, projected at the outer midplane for various dRsep values. DRsep is varied from LSN (dRsep = -5 mm, black) to dRsep = +16 mm (orange) and scanning through -2.5 (red), +4.5 (green), +6 (blue), +9 (purple) and +13 mm (light blue). Heat flux derived from FRP is indicated by the blue/white square. The private flux region (PFR) and the SOL are shown, with the dashed line indicating the separatrix of the LSN.

The ELM heat flux profiles of the LSN case (black in *Fig. 5*) show a peak value at the outer target of ~1500 W/cm^2, almost comparable in magnitude to ~1100 W/cm^2 at the inner target and this persists as dRsep is varied and will be discussed in more detail later.

When the magnetic configuration is changed from LSN to USN, and a secondary divertor forms at the floor, heat flux profiles shift outwards in both inner and outer targets and the peak values at the outer divertor drop with increasing dRsep. When dRsep > 10mm, the inner divertor profiles decrease to background level while the outer ones still feature some flux. Notice that the inner divertor profiles are well defined whereas the outer divertor profiles feature ripples that do not quite decay even at dRsep = +16mm. Similar features have been previously observed[45] for SN discharges and [26] for DN configuration, together with rippled structures located at the outer part of the profile[28].

Some understanding of the profiles shown in *Fig. 5* can be achieved by considering that the ELM has a ballooning nature and thus starts as filaments bulging from the low field side (LFS)[46][47] separatrix that are eventually ejected into the SOL from where the plasma is transported along the field lines to the primary divertor outer target, and around the plasma crown to the primary divertor inner target. The outward shifting of secondary divertor heat flux peaks can be understood inspecting *Fig. 6*. As the ELM plasma (sketched in red in *Fig. 6a*) travels or expands radially away from the separatrix, mostly flowing to the primary divertor over the crown, it eventually reaches flux surfaces that intersect the secondary outer divertor, resulting on heat flux profiles that shift in the

normalized poloidal flux surface space (Ψ_n), as indicated in *Fig. 6b* and *6c*. Such shift is observed in *Fig. 5* as the secondary divertor forms (dRsep > 0).

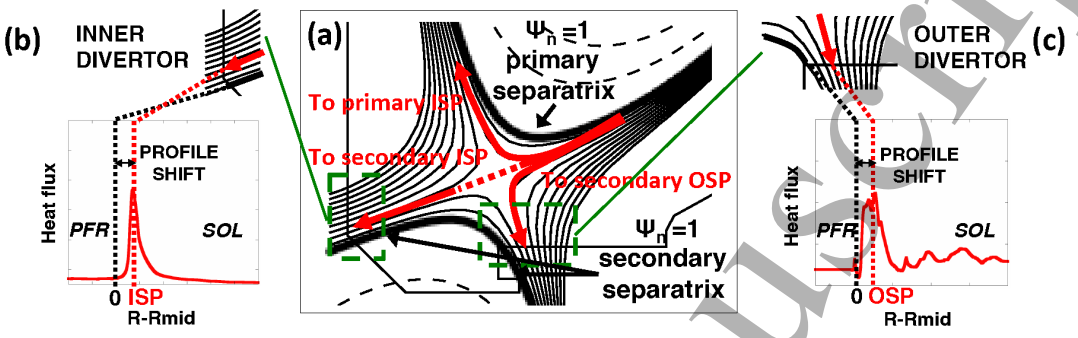

Figure 6 (a) Visual representation of the plasma path at a secondary XPT in DIII-D. Heat flux to the primary ISP, secondary ISP and OPS are highlighted. The thick black lines indicate the normalized poloidal flux surfaces (Ψ_n) of primary and secondary separatrices, which result in R-Rmid = 0 when mapped to the outer midplane. (b) Zoom of the ISP, with the profile shift shown. (c) Zoom of the OSP, with the profile shift shown.

We are not aware of a theoretical explanation for how the ELM pulse crosses the flux surfaces and arrives at the secondary inner strike point, but magnetic reconnection or related phenomena may be involved. The shifts observed in *Fig. 5* correspond to the distance between the secondary separatrix (indicated by a thick black line in *Fig. 6a*, *6b* and *6c*), where $\Psi_n = 1$, and the secondary strike points (indicated with a dashed red line in *Fig. 6b* and *6c*), mapped at the outer midplane. Therefore, significant heat flux at the secondary divertor is observed at both the outer and inner targets (*Fig. 5*) and the magnitude of such flux is a significant fraction to that to the primary divertor, as we will quantify and discuss later.

The IRTV and the fast probe overlap in spatial coverage in the outer divertor for some time windows, and therefore we can cross-check the transient ELM heat flux measured by both. The heat flux q can be calculated from probe data taken near the floor by using the standard sheath formula[48]: $q = \gamma k_b T_e \frac{J_{sat}}{e}$, using the value of electron temperature, T_e and saturation current, J_{sat} and with the sheath heat transmission coefficient, γ ,set at 7. The result, shown as a blue/white square in *Fig. 5*, is consistent with the IRTV measurement. It was not possible to extend such measurements closer to the separatrix due to arcs occurring on the probe tips during ELMs.

In order to quantify the heat flux distribution among divertors, the conditionally-averaged ELM heat flux profiles (*Fig. 5*), have been radially integrated over the IRTV view R,Z coordinates of inner and outer divertors, with the total integrated heat flux to the lower divertor given by $Q_{tot} = \int q_{inner} dr + \int q_{outer} dr$. Results are reported in *Table 2*.

Table 2 Radially integrated ELM heat flux to inner and outer lower divertor.

dRsep (mm)	Q_i (W/cm)	Q_o (W/cm)	Q_{SUM} (W/cm)
-5	8707	30668	39375
-2.5	7702	27963	35666
+4.5	2070	17432	19502
+6	1999	17095	19094
+9	1671	15740	17411
+13	275	14369	14644
+16	203	13607	13810

Inspecting the data in *Table 2*, the secondary divertor, with dRsep of +4.5 and +6mm, receives about 1/3 of the total ELM heat flux deposited to a primary divertor in a well-defined SN, while that fraction drops below ~1/4 when dRsep = +16mm. The total SN ELM heat flux is extracted from our data by summing the flux of two magnetically symmetric discharges, as $Q_{SN} = \int q_{tot(dRsep=-5mm)} dr + \int q_{tot(dRsep=+4.5mm)} dr$ i.e. ~58,880 W/cm.

The values presented in *Table 2* are shown in *Fig. 7a*, together with the peak values of the same profiles (*Fig. 7b*).

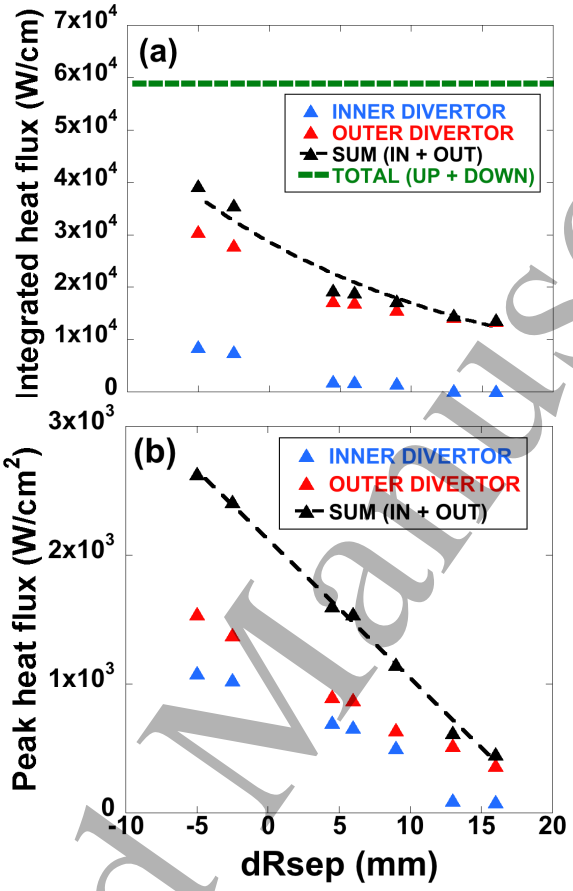

Figure 7 (a) Radially-integrated ELM heat flux profiles reported in *Fig. 5* for several values of dRsep. The total (up+down) flux is indicated with a green dashed line for comparison. (b) Peak values of the same profiles.

The radially integrated heat flux data (indicated in black in *Fig. 7a*), dominated by the outer divertor, displays an exponential decay with the resulting fit function being $Q_{int}(dRsep) = 2.87\times10^{4} * e^{-0.052*dRsep}$. We estimate that dRsep needs to be increased beyond ~25-30mm to bring the heat flux to the secondary divertor below 10% of the total heat flux driven by an ELM to an actual SN (indicated with a green dashed line in *Fig. 7(a)*).

The dRsep uncertainty on the primary and secondary divertor power sharing in DIII-D is about 2mm[49], which corresponds to a difference on the total heat flux (green in Fig. 7a) of ~2900 W/cm, giving an estimated error of about 5%. ELM-induced reflection may also be a concern on the IR measurements; however, this effect is expected to be negligible in carbon wall machines compared to metal walls ones[50], given the low emissivity of W (ε~0.2-0.3) compared to graphite (ε~0.8-0.9). An ELM-resolved power balance $\Delta W_{target} = \Delta W_{plasma} + \Delta W_{in} - \Delta W_{rad}$ where $\Delta W_{target} = \mathrm{W_{ELM(IR)}} 2\pi R dt$ with $dt = 1.3ms$ (the averaged ELM duration), $\mathrm{W_{ELM(IR)}} = 58{,}880$ (green in Fig. 7a), $\Delta W_{in} = 4.8kJ$ and $\Delta W_{rad} = 5kJ$ (averaged over 5ms), gives a deposited energy of

~75kJ. The discrepancy with the average ΔW_{ELM} (~60 kJ), or 20%, is within the data scatter of the IRTV, the diamagnetic measurement and observed ELM[47][51] heat deposition toroidal asymmetries[52][28].

The peak heat flux (*Fig. 7b*) shows a linear decay with a slope of -107.5*dRsep and an almost even load between the inner and outer divertor for 0<dRsep<+10mm. The data highlights that the radial profile has a significant effect on the total heat received by the secondary divertor, in particular that significant amount of heat flux is received from the far SOL at the outer target, (*Fig. 5,* right), whereas the inner target sees little far SOL flux (*Fig. 5*, left).

Inter-ELM time-averaged heat flux has also been calculated and the resulting profiles, mapped at the outer midplane, are shown in *Fig. 8*.

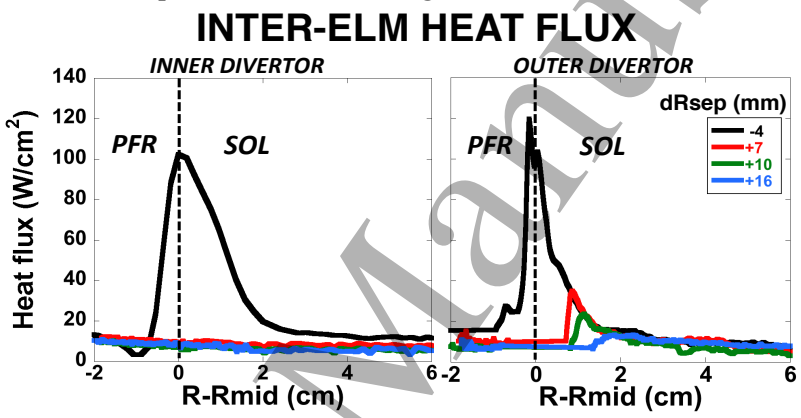

Figure 8 Lower divertor inter-ELM time-averaged heat flux for inner (left) and outer (right) divertor, projected at the midplane. DRsep is varied from LSN (dRsep = -4 mm, black) to dRsep = +16 mm (blue) and scanning through +7 (red) and +10 mm (green). The PFR and the SOL are shown, with the dashed line indicating the separatrix of the LSN.

LSN profiles (black curves in *Fig. 8*) exhibit a broader shape at the inner target and similar peak values between inner and outer targets. It is important to note that the toroidal field was reversed in these experiments, with ∇B ion drift directed away from the LSN configuration, which leads to more symmetric heat loads between inner and outer regions[53][54]. Similarly to what has been observed in Alcator C-MOD[25] and ASDEX-Upgrade[28], the inter-ELM heat flux to the secondary inner target is small for all dRsep cases, thus confirming that the heat flux measured at the inner target in *Fig. 5* is driven by ELMs.

3.2 Particle flux to the secondary divertor and plasma recycling

We measured the particle flux to the lower outer divertor during ELMs and inter-ELM for various values of dRsep using the divertor reciprocating probe. The flux is given by the relation $\Gamma_i = \frac{J_{sat}}{e}$, where J_{sat} is the ion saturation current density, and the results are shown in *Fig. 9* as a function of R-Rsep, mapped to the outer midplane.

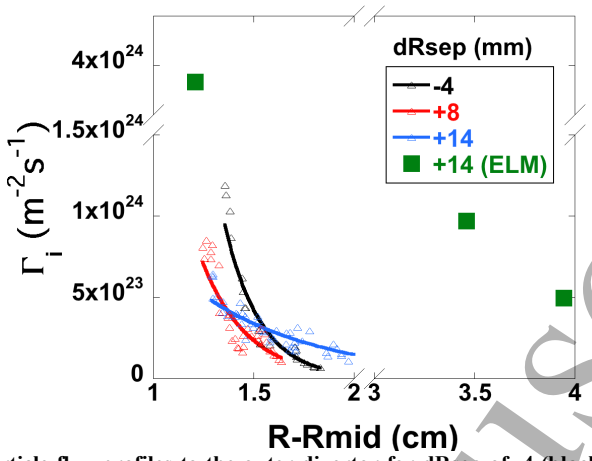

Figure 9 Inter-ELM particle flux profiles to the outer divertor for dRsep of -4 (black, LSN), +8 (red) and +14 (blue), both USN. ELM-driven flux, available only for dRsep = +14mm, is indicated in green. Solid lines are exponential fits to the data. The separatrix is at R-Rmid=0 (not shown).

Inter-ELM data (black, red and blue in *Fig. 9*) have been fitted with an exponential of the form $\Gamma_{i(R-Rmid)} = \Gamma_i(0) * e^{-\lambda(R-Rmid)}$.The LSN case (black) displays a steep decay, with $\lambda = -5.6$, compared to the USN cases (red and blue), whose λ coefficients are -4.3 and -1.7 respectively. Hence, the inter-ELM particle flux is quickly reduced by ~70% with an increase in dRsep of 12mm, and spreads over a larger area in the divertor. The ELM particle flux (green in *Fig. 9*) is at least 6 times higher compared to inter-ELM (dRsep = +14mm) and a significant amount is collected from the far SOL, which is consistent with the IRTV measurements.

ELM-induced plasma recycling has been evaluated by measuring D-α emissions at the lower and upper divertor simultaneously. The D-α signal is proportional to the density of ground-state recycled atoms and can therefore provide indirect information on the plasma flux and recycling to the walls. The normalized D-α signal, absolutely calibrated hence providing accurate relative emission, during the ELM peaks and averaged over several ELMs, together with the divertor regions of interest, are shown in *Fig. 10*.

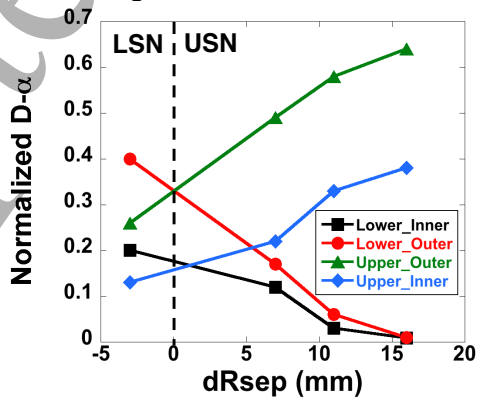

Figure 10 Normalized D-alpha signals during an ELM from both lower and upper divertor is plotted vs dRsep of -3, +7, +11 and +16mm.

The emission is larger at the primary outer divertor for all cases. The lower inner divertor signal is still significant when dRsep < 10mm, confirming that ELM plasma reaches the secondary inner divertor region. Emissions from the secondary divertor (inner + outer) are below ~15% of the total when dRsep > 10mm.

Uncertainties regarding D-α sources are related to molecule-activated recombination processes involving D_2 and C_xD_y as well as different geometries and neutral concentrations characterizing the lower and upper divertors in DIII-D[55]. Moreover, filterscope chords are in discrete locations that, therefore, do not necessarily align with the strike points spatial coordinates. However, findings in *Fig. 10* are in line with IRTV measurements i.e. the secondary divertor collects up to 1/3 of the ELM energy, when dRsep < 10mm.

4. Conclusions

Heat and particle flux to primary and secondary divertors in ELMing H-mode attached discharges at DIII-D tokamak have been evaluated, during ELMs and inter-ELM, keeping plasma parameters identical and varying only dRsep. IRTV has been used to measure heat loads and a fast reciprocating probe and filterscopes to evaluate particle flux and plasma recycling. The main results can be summarized as follows:

- The heat flux to the secondary divertor is significant during ELMs, up to 1/3 of the total (primary+secondary) ELM heat flux. Between ELMs, however, the secondary divertor peak heat flux remains below 25% of the primary divertor.
- The secondary inner divertor receives up to ~50% of the ELM peak heat flux to the secondary divertor (inner + outer), albeit ~10% of the total integrated ELM heat flux. Thus, we have experimentally verified that significant ELM plasma is deposited to the secondary inner target, resulting in well-defined profiles that are shifted from the secondary ISP.
- The ELM heat flux to the secondary outer divertor spreads widely over the SOL. This is consistent with previous studies from other machines[26][28] and confirmed here also by the significant amount of ELM particle flux measured in the far SOL.
- The radially-integrated ELM heat flux to the secondary divertor, larger at the outer divertor, decays exponentially, flattening out at larger dRsep and implying that dRsep needs to be at least ~25-30mm to reduce the flux to 10% of the total ELM-driven heat flux deposited to a well-defined SN. The peak heat flux to the secondary divertor decays linearly and much more rapidly than the total heat flux when dRsep is large.

Good control on the up-down magnetic balance in future fusion machines will be vital in order to protect the divertor walls, including regions surrounding both the secondary inner and outer strike points. Spatially-resolved ELM simulations for unbalanced DN configurations are needed in order to shed light on the mechanism transporting ELM plasma to the secondary inner divertor target.

5. Acknowledgments

Supported by the US DOE under Contract No. DE-FC02-04ER54698 and Grant No. DE-FG02-07ER54917. The authors are thankful for enlightening discussions with Dr. R. A. Pitts.

6. Disclaimer

7. References

[1] P.B. Snyder et al., Phys. Plasmas 9 (2002) 5
[2] F. Wagner et al., Phys. Rev. Lett. 49 (1982) 19
[3] D.N. Hill, J. Nucl. Mater. 241-243 (1997)
[4] J.A. Boedo et al., Phys. Plasmas 12 (2005) 072516
[5] M. Knolker et al., Nucl. Fusion 58 (2018) 096023
[6] A.W. Leonard, Phys. Plasmas 21 (2014) 090501
[7] www.iter.org
[8] F. Escourbiac et al., Fusion Eng. Des. 146 (2019) 2036-2039
[9] R.A. Pitts et al., Nucl. Mater. Energy 20 (2019) 100696
[10] J.W. Coenen et al., Nucl. Fusion 51 (2011) 083008
[11] R.A. Pitts et al., J. Nucl. Mater. 438 (2013) S48-S56
[12] G. Pintsuk et al., Fusion Eng. Des. 82 (2007) 1720-1729
[13] R. Maingi et al., Nucl. Fusion 51 (2011) 063036
[14] T. Evans et al., Nature Physics 2 (2006) 419-423
[15] D.D. Ryutov et al., Phys. Plasmas 22 (2015) 110901
[16] T.D. Rognlien et al., J. Nucl. Mater. 438 (2013) S418-S421
[17] P.M. Valanju et al., Phys. Plasmas 16 (2009) 056110
[18] S.F. Smith et al., 46th EPS Conference on Plasma Physics (2019) P2.1037
[19] R. Marchand et al., Nucl. Fusion 35 (1995) 297
[20] M. Kocan et al., J. Nucl. Mater. 463 (2015) 709-13
[21] R.A. Pitts et al., J. Nucl. Mater. 415 (2011) S957-S964
[22] A. Sykes et al., Nucl. Fusion 58 (2018) 016039
[23] S.C. Liu et al., Phys. Plasmas 19 (2012) 042505
[24] L. Wang et al., Nucl. Fusion 54 (2014) 114002
[25] D. Brunner et al., Nucl. Fusion 58 (2018) 076010

[26] G. De Temmerman et al., J. Nucl. Mater. 415 (2011) S383-S386
[27] A. Herrmann et al., J. Nucl. Mater. 290-293 (2001) 619-622
[28] T. Eich et al., Plasma Phys. Control. Fusion 47 (2005) 815
[29] A.C.C. Sips et al., Plasma Phys. Control. Fusion 44 (2002) B69-B83
[30] M. Faitsch et al., Nucl. Mater. Energy 26 (2021) 100890
[31] G. Saibene et al., Nucl. Fusion 45 (2005) 297-317
[32] C.J. Lasnier et al., J. Nucl. Mater. 290-293 (2001) 1093-1096
[33] T.W. Petrie et al., Nucl. Fusion 43 (2003) 910-913
[34] J. Watkins et al., 23rd IAEA Fusion Energy conference (2010), Report n. IAEA-CN—180.
[35] H. Anand et al., Nucl. Fusion 60 (2020) 036011
[36] L.L. Lao et al., Nucl. Fusion 25 (1985) 1611
[37] C.J. Lasnier et al., Nucl. Fusion 38 (1998) 1225
[38] A. Herrmann et al., Plasma Phys. Control. Fusion 37 (1995) 17
[39] J.G. Watkins et al., Rev. Sci. Inst. 68 (1997) 373
[40] J.A. Boedo et al., Rev. Sci. Inst. 69 (1998) 2663
[41] J.A. Boedo et al., Phys. Plasmas 8 (2001) 4826
[42] P.C. Stangeby, J. Nucl. Mater. 145-147 (1987) 105-116
[43] R.J. Colchin et al., Rev. Sci. Inst. 74 (2003) 2068
[44] S. Jachmich et al., 36th EPS Conference on Plasma Phys. 33E (2009) P-2.159
[45] A. Kallenbach et al., Nucl. Fusion 48 (2008) 085008
[46] P.B. Snyder et al., Phys. Plasmas 9 (2002) 2037
[47] J.A. Boedo et al., Phys. Plasmas 12 (2005) 072516
[48] P.C. Stangeby, The Plasma Boundary of Magnetic Fusion Devices, IoP Publishing Ltd 2000
[49] T.W. Petrie et al., J. Nucl. Mater. 290-293 (2001) 935-939
[50] Ph. Lotte et al., Rev. Sci. Instrum. 81 (2010) 10E120
[51] A.W. Leonard et al., GA internal communication GA-A22346 (1997)
[52] T.E. Evans et al., J. Nucl. Mater. 220-222 (1995) 235-239
[53] A.V. Chankin et al., Plasma Phys. Control. Fusion 38 (1996) 1579
[54] N. Asakura et al., J. Nucl. Mater. 220-222 (1995) 395-399
[55] L. Casali et al., Nucl. Fusion 60 (2020) 076011